npj | quantum information

Article

Published in partnership with The University of New South Wales

https://doi.org/10.1038/s41534-025-01108-8

Hole spin qubits in unstrained Germanium layers

Lorenzo Mauro, Mauricio J. Rodríguez, Esteban A. Rodríguez-Mena & Yann-Michel Niquet

Strained germanium heterostructures are one of the most promising material for hole spin qubits but suffer from the strong anisotropy of the gyromagnetic factors that hinders the optimization of the magnetic field orientation. The figures of merit (Rabi frequencies, lifetimes…) can indeed vary by an order of magnitude within a few degrees around the heterostructure plane. We propose to address this issue by confining the holes at the interface of an unstrained, bulk Ge substrate or thick buffer. We model such structures and show that the gyromagnetic anisotropy is indeed considerably reduced. In addition, the Rabi frequencies and quality factors can be significantly improved with respect to strained heterostructures. This extends the operational range of the qubits and shall ease the scale-up to many-qubit systems.

Hole spin qubits in semiconductor quantum dots have made remarkable progress as a compelling platform for quantum computing and simulation[1–6]. One of their main assets is the efficient electrical manipulation enabled by the strong spin-orbit coupling (SOC) in the valence bands of semiconductor materials[7–11]. In particular, planar germanium heterostructures now stand out as the state-of-the-art material for hole spin qubits[12,13]. The quality of epitaxial interfaces indeed reduces the disorder around the qubits[14–17], and the small effective mass of holes in Ge allows for larger quantum dots, which eases fabrication and integration. High-fidelity single and two-qubit gates have thus been reported in germanium heterostructures[18–23], in up to ten qubits[24]. Singlet-triplet spin qubits[25–28], manipulation by spin shuttling[29], and quantum simulation[30] have also been demonstrated on this platform.

In these heterostructures, the heavy-hole (HH) and light-hole (LH) subbands are strongly split by the biaxial strains resulting from the growth on a mismatched GeSi buffer[12]. As a consequence, the low-lying hole states have strong HH character, and thus show a highly anisotropic gyromagnetic response, with in-plane g-factors $g_\parallel \lesssim 0.5$ and out-of-plane g-factors $g_\perp \gtrsim 10$[23]. Therefore, all relevant spin properties (Larmor and Rabi frequencies, lifetimes, …) vary rapidly (over $\approx 1°$) when the magnetic field crosses the heterostructure plane where these devices are usually operated[31]. Optimizing the magnetic field orientation for best performances (Rabi frequencies, quality factors and fidelities, …) can thus be challenging, especially in many-qubit systems with significant dot-to-dot variability. Moreover, the small HH/LH mixing limits the maximum Rabi frequencies achieved in these devices.

It would, therefore, be desirable to increase the HH/LH mixing and reduce the g-factor anisotropy. As discussed in ref. 32, this may be achieved with strain engineering, but a scalable design is still lacking. An alternative solution is to host the qubits in a bulk Ge substrate insulated from the gate stack by a thin, strained GeSi barrier[33,34]. The quantum dots are then accumulated at the Ge/GeSi interface by the electric field from the gates. As the Ge substrate is unstrained, the HH/LH band gap is expected significantly smaller and the HH/LH mixing much stronger[35]. The growth of such a structure, with the formation of a high mobility hole gas at the interface, has actually been demonstrated very recently[36].

In this work, we explore the prospects for unstrained bulk Ge qubits with detailed numerical simulations. We analyze the dependence of the g-factors on the electrical confinement, and show that the g-factor anisotropy can indeed be significantly reduced even for moderate HH/LH mixings. The stronger mixing increases the average Rabi frequencies f_R and dephasing rates $1/T_2^*$; nonetheless, the quality factor $Q_2^* = 2f_\mathrm{R}T_2^*$ can be larger than in strained heterostructures. Most importantly, the dependence of these quantities on the magnetic field orientation is much broadened, allowing for an easier optimization of the operating point in many-qubit systems. We discuss the implications for the development of hole spin qubit technologies.

Results

Device and methodology

In order to compare strained and unstrained Ge qubits, we consider the same prototypical device as in refs. 37,38 (see Fig. 1). The heterostructure comprises a Ge well with thickness L_w laid on $\mathrm{Ge}_{0.8}\mathrm{Si}_{0.2}$ and capped with a 20 nm-thick $\mathrm{Ge}_{0.8}\mathrm{Si}_{0.2}$ barrier. We address two hypotheses: *i*) the whole heterostructure is grown coherently on a thick $\mathrm{Ge}_{0.8}\mathrm{Si}_{0.2}$ buffer with a small, residual in-plane strain $\varepsilon_\mathrm{buf} = 0.26\%$. The Ge well then undergoes compressive biaxial strains $\varepsilon_{xx} = \varepsilon_{yy} = \varepsilon_\parallel = -0.61\%$ and $\varepsilon_{zz} = \varepsilon_\perp = 0.45\%$. These settings are representative of the experimental, strained Ge heterostructures[12]; *ii*) the Ge well is unstrained but the $\mathrm{Ge}_{0.8}\mathrm{Si}_{0.2}$ layers undergo tensile strains $\varepsilon_{xx} = \varepsilon_{yy} = 0.87\%$ and $\varepsilon_{zz} = -0.66\%$. The bulk

Univ. Grenoble Alpes, CEA, IRIG-MEM-L_Sim, Grenoble, France. e-mail: yniquet@cea.fr

germanium device is then the limit $L_w \to \infty$. Although only this bulk device is practically relevant, finite L_w's provide valuable insights into the physics of the device. In both cases, the barrier at the Ge/GeSi interface is $\Delta E_{\rm HH} \approx 140$ meV for HH states and $\Delta E_{\rm LH} \approx 80$ meV for LH states.

The difference of potential between a central C gate and side L, R, T, and B gates on top of the heterostructure shapes a quantum dot in the Ge well. The device is placed in a magnetic field $\mathbf{B}$ whose orientation is characterized by the polar (out-of-plane) angle θ with respect to $z = [001]$, and by the azimuthal (in-plane) angle φ with respect to $x = [100]$. The spin of a single hole trapped in the quantum dot is manipulated with radio-frequency signals applied either to the central or side gates. We compute the potential created by the gates with a finite volumes Poisson solver, then the wave function of the hole with a finite-differences discretization of the Luttinger-Kohn Hamiltonian[37–40] (see Methods). We finally calculate the Larmor and Rabi frequencies of the spin with the g-matrix formalism[41]. We do not account here for the inhomogeneous strains imprinted by the differential thermal contraction of the materials when the device is cooled down[38]. The latter are discussed in the Supplementary Information.

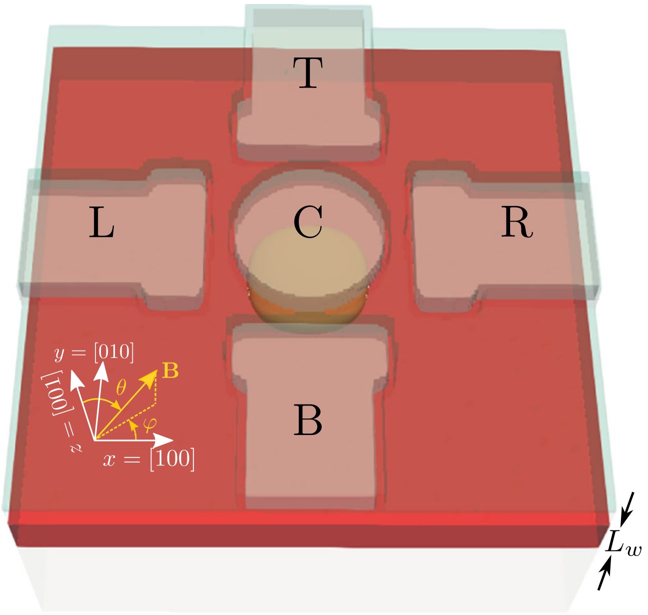

Fig. 1 | The test device is made of a Ge well (red) with thickness L_w ranging from 10 nm to $L_w \to \infty$ (bulk). It is capped with a 20-nm-thick $\rm Ge_{0.8}Si_{0.2}$ barrier (blue). The dot is shaped by five Al gates (gray) embedded in 5 nm of $\rm Al_2O_3$. The diameter of the central gate is $d = 100$ nm. The yellow shape illustrates the location and shape of the quantum dot. The orientation of the magnetic field $\mathbf{B}$ is characterized by the angles θ and φ in the crystallographic axes set $x = [100]$, $y = [010]$ and $z = [001]$.

Dimensions and *g*-factors of the dots

The effective Hamiltonian of the hole spin can be written $H = \frac{1}{2}\mu_B \boldsymbol{\sigma} \cdot \hat{g}\mathbf{B}$, where μ_B is Bohr's magneton, $\boldsymbol{\sigma}$ is the vector of Pauli matrices and $\hat{g}$ is the gyromagnetic matrix[41]. For quantum dots with quasi-circular symmetry, this matrix is diagonal, with principal g-factors $g_{xx} = -g_{yy} = g_\parallel$, and $g_{zz} = g_\perp$[37,38].

The principal g-factors $g_\parallel$ and $g_\perp$ are plotted as a function of the well thickness L_w in Fig. 2 for both strained and unstrained Ge wells. The potential applied to the central gate is $V_{\rm C} = -10$ mV and the side gates are grounded. The vertical extension $\ell_\perp = \sqrt{\langle z^2\rangle - \langle z\rangle^2}$ and the lateral extension $\ell_\parallel = \sqrt{\langle x^2\rangle} = \sqrt{\langle y^2\rangle}$ of the dot are also shown in this figure.

As expected, the vertical extension of the dot increases with L_w, but is ultimately limited by the vertical electric field from the gates that tends to squeeze the hole at the top $\rm Ge/Ge_{0.8}Si_{0.2}$ interface. Indeed, $\ell_\perp \approx 0.18L_w$ is consistent with a square well model for small L_w, but departs from this trend in thick Ge films. There is little difference between strained and unstrained wells as the biaxial strain has almost no effect on the vertical confinement mass. The dot also extends laterally with increasing L_w, primarily because the in-plane (transport) mass of the hole decreases (from $m_\parallel \approx 0.08\, m_0$ for $L_w = 10$ nm to $m_\parallel \approx 0.06\, m_0$ for $L_w = 70$ nm, with m_0 the free electron mass) (To lowest order, the transport mass is $m_\parallel \approx m_0/(\gamma_1 + \gamma_2 - \gamma_h)$, where $\gamma_1 = 13.18$, $\gamma_2 = 4.24$ and γ_h is defined after Eq. (2)[42]). This is also why the dots are more localized in the unstrained Ge wells that exhibit heavier transport masses ($m_\parallel \approx 0.1\, m_0$ for $L_w = 10$ nm and $m_\parallel \approx 0.08\, m_0$ for $L_w = 70$ nm).

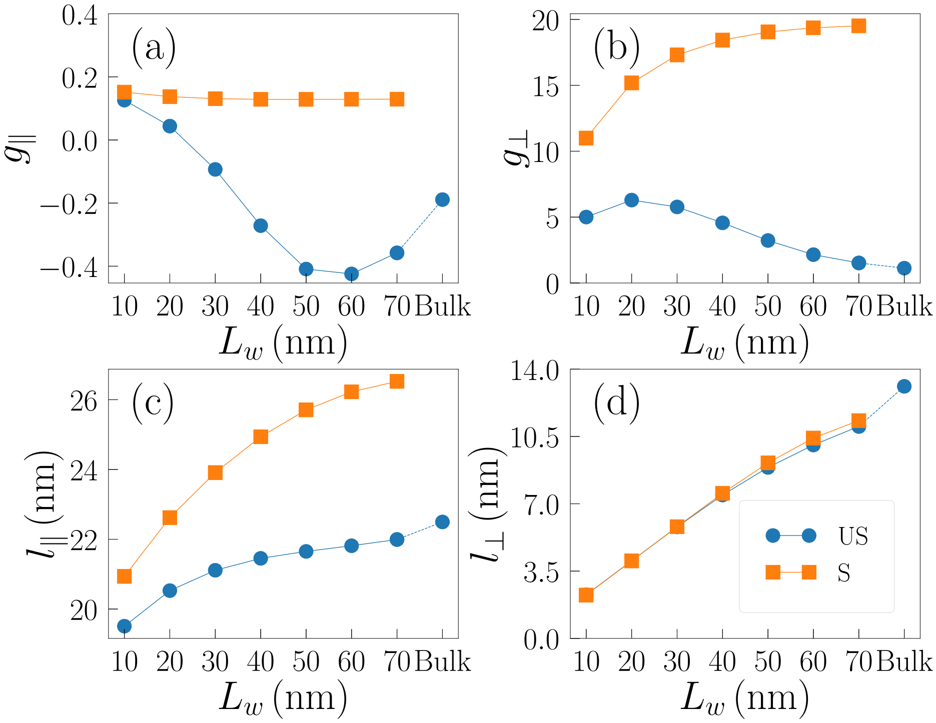

Fig. 2 | g-factors and extensions of the dot as a function of well thickness. a, b g-factors $g_\parallel$ and $g_\perp$ as a function of the thickness L_w of strained (S) and unstrained (US) Ge wells. **c, d** In-plane extension $l_\parallel$ and out-of-plane extension $l_\perp$ of the dot as a function of L_w. All calculations are performed at $V_{\rm C} = -10$ mV with the side gates grounded.

Although undesirable, the enhanced localization in unstrained Ge wells remains limited.

The gyromagnetic factors follow very different trends in strained and unstrained Ge wells. In particular, the g-factor anisotropy $g_\perp/g_\parallel$ is much reduced in bulk Ge, as a result of the enhancement of the HH/LH mixing. Indeed, the g-factors of a pure HH state are $g_\parallel = 3q = 0.18$ and $g_\perp = 6\kappa + 27q/2 = 21.27$, while those of a pure LH state are $g_\parallel \approx 4\kappa = 13.64$ and $g_\perp \approx 2\kappa = 6.82$ (with $\kappa = 3.41$ and $q = 0.06$ the isotropic and cubic Zeeman parameters of Ge). The confinement and magnetic vector potential admix LH components into the HH ground-state; to lowest order in perturbation, the g-factors of the dot then read[37,38,42]

$$g_\parallel \approx 3q + \frac{6}{m_0\Delta_{\mathrm{LH}}}\left(\lambda\langle p_x^2\rangle - \lambda'\left\langle p_y^2\right\rangle\right) \tag{1}$$

$$g_\perp \approx 6\kappa + \frac{27}{2}q - 2\gamma_h, \tag{2}$$

where $\lambda = \kappa\gamma_2 - 2\eta_h\gamma_3^2$ and $\lambda' = \kappa\gamma_2 - 2\eta_h\gamma_2\gamma_3$, with $\gamma_2 = 4.24$ and $\gamma_3 = 5.69$ the Luttinger parameters of bulk Ge[7,38]. Δ_{LH} is the HH/LH bandgap and $p^2 = \langle p_x^2\rangle = \langle p_y^2\rangle \propto 1/\ell_\parallel^2$ are the expectation values of the squared in-plane momentum operators over the ground-state HH envelope. The factors γ_h and η_h depend on vertical confinement and describe the action of the magnetic vector potential on the orbital motion of the holes[42,43]. For small vertical electric fields, Δ_{LH} can be approximated as[42]

$$\Delta_{\mathrm{LH}} \approx \frac{2\pi^2\hbar^2\gamma_2}{m_0 L_w^2} + 2b_v(\varepsilon_\parallel - \varepsilon_\perp), \tag{3}$$

where the first term $\Delta_{\mathrm{LH}}^{(c)}$ accounts for vertical confinement and the second term $\Delta_{\mathrm{LH}}^{(s)}$ accounts for biaxial strains, with $b_v = -2.16$ eV the uniaxial deformation potential of the valence band (This expression is not valid for large L_w's where the confinement becomes electrical and $\Delta_{\mathrm{LH}}^{(c)} \propto 1/\ell_\perp^2$. We use it as a guide in the present, qualitative discussion.).

In strained Ge wells, $\Delta_{\mathrm{LH}}^{(s)} = 46$ meV is large and overcomes confinement ($\Delta_{\mathrm{LH}}^{(c)} \approx 25$ meV at $L_w = 15$ nm) except for the smallest L_w's. As a consequence, the total weight $m^2 \propto (p^2/\Delta_{\mathrm{LH}})^2$ of the LH components in the hole ground-state is < 0.2%, as shown in Fig. 3. The HH/LH mixing actually weakens with increasing L_w because p^2 diminishes faster than Δ_{LH}. Owing to the large Δ_{LH} and dot sizes, $g_\parallel \approx 3q$, while $g_\perp$ decreases when thinning the well due to the dependence of γ_h on vertical confinement[42].

On the opposite, $\Delta_{\mathrm{LH}} \equiv \Delta_{\mathrm{LH}}^{(c)}$ is much smaller in unstrained Ge wells so that the HH/LH mixing is significantly stronger. As a matter of fact, m^2 increases continuously with L_w and reaches ≈ 17.5% when $L_w \to \infty$. The effect on the out-of-plane g-factor is impressive, $g_\perp$ being as small as 1.13 in the bulk device. This is actually much smaller than expected for a pure light-hole due to the complex interplay between the confinement and the magnetic spin and orbital Hamiltonians. This strong decrease of $g_\perp$ has been demonstrated experimentally (and theoretically) in a 2D hole gas in ref. 36. On the other hand, the in-plane g-factor remains small and shows a non-monotonic behavior with increasing L_w. The change of sign of $g_\parallel$ around $L_w = 25$ nm is qualitatively consistent with the closing of the HH/LH bandgap, thus the increase of the $\propto(\lambda - \lambda') < 0$ correction in Eq. (1)[37,38]. We emphasize, though, that this expression is not quantitative for mixings $m^2 \gtrsim 1\%$. The bounce at large L_w is in particular due to the higher order terms not captured by Eq. (1). At very large mixing, $g_\parallel$ shall tend to the in-plane g-factor $4\kappa = 13.64$ of a pure light-hole.

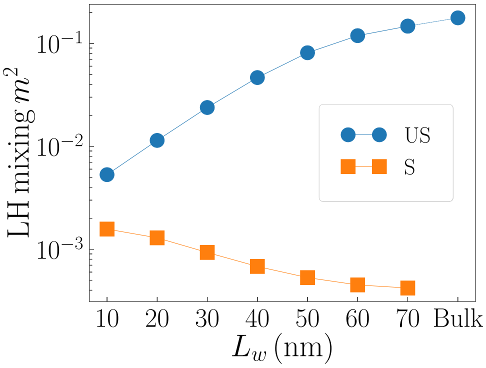

Fig. 3 | Weight m^2 of the LH components in the ground-state hole wave function, as a function of the thickness L_w of strained (S) and unstrained (US) Ge wells ($V_{\mathrm{C}} = -10$ mV).

We finally discuss the dependence of the g-factors on the gate voltage V_{C} in the unstrained, bulk device. The dot extensions, g-factors, and HH/LH mixing in this device are plotted as a function of V_{C} in Fig. 4. As expected, the dot shrinks when V_{C} is pulled down, because the vertical and lateral components of the electric field are both $\propto V_{\mathrm{C}}$. As a consequence, the HH/LH bandgap opens, but the strength ($\propto p^2$) of the HH/LH couplings increases, so that the g-factors vary rather slowly. The in-plane g-factor saturates to $g_\parallel \approx -0.3$ at high electric field. We further address in the Supplementary Information how the in-plane g-factors depend on the ellipticity of the dots (allowing, e.g., spin manipulation by shuttling)[29].

Spin manipulation

We characterize spin manipulation with a given gate by the Rabi frequency f_{R} and by the quality factor $Q_2^* = 2f_{\mathrm{R}}T_2^*$ (the number of π rotations that can be achieved within the electrical dephasing time T_2^*). The Rabi frequency is computed from the g-matrix as[41]

$$f_{\mathrm{R}} = \frac{\mu_B|\mathbf{B}|V_{\mathrm{ac}}}{2hg^*}|(\hat{g}\mathbf{b}) \times (\hat{g}'\mathbf{b})|, \tag{4}$$

where $\mathbf{b} = \mathbf{B}/|\mathbf{B}|$, $g^* = |\hat{g}\mathbf{b}|$ is the effective g-factor, $\hat{g}'$ is the derivative of $\hat{g}$ with respect to the driving gate voltage, and V_{ac} is the amplitude of the drive. To compute T_2^*, we lump as in refs. 31,32 all electrical fluctuations into effective gate voltage noises:

$$\frac{1}{T_2^*} = \Gamma_2^* = \sqrt{2}\pi\sqrt{\sum_{\mathrm{G}}\left(\delta V_{\mathrm{rms}}\frac{\partial f_{\mathrm{L}}}{\partial V_{\mathrm{G}}}\right)^2}. \tag{5}$$

The sum runs over the gates G ∈ {C, L, R, T, B}, $f_{\mathrm{L}} = \mu_B g^*|\mathbf{B}|/h$ is the Larmor frequency, δV_{rms} is the rms amplitude of the noise (assumed the same on all gates), and $\partial f_{\mathrm{L}}/\partial V_{\mathrm{G}}$ is the longitudinal spin electric susceptibility (LSES) of gate G (also a function of the corresponding $\hat{g}'$)[31,44,45]. Q_2^* is independent on $B = |\mathbf{B}|$ and is proportional to the ratio $\rho_{\mathrm{ac}} = V_{\mathrm{ac}}/\delta V_{\mathrm{rms}}$ between the drive and noise amplitudes. We set $\rho_{\mathrm{ac}} = 100$ in the following (in order-of-magnitude agreement with ref. 24). We discuss the hyperfine dephasing rate, as well as the spin-phonon relaxation time T_1 (which does not limit the operation of the qubits at $f_{\mathrm{L}} \lesssim 1$ GHz) in the Supplementary Information.

The maps of the LSES, Rabi frequency and quality factor of the C and L gates are shown in Fig. 5 for the unstrained, bulk Ge device. The gate voltage is $V_{\mathrm{C}} = -25$ mV and the principal g-factors are $g_\parallel = -0.28$ and $g_\perp = 1.01$ ($|g_\perp/g_\parallel| = 3.61$). The Rabi frequencies are plotted at constant Larmor frequency $f_{\mathrm{L}} = 1$ GHz. The maps of the B, R and T gates can be deduced from those of the L gate by rotations $\delta\varphi = 90$, 180, and 270°, respectively. The C gate modulates $\ell_\parallel$ and $\ell_\perp$ but does not break the symmetry of the dot, which only changes the diagonal g-factors $g_\parallel$ and $g_\perp$ ($g_\parallel' = 2.11$ V^{-1} and $g_\perp' = 3.5$ V^{-1}). This has no effect on the spin precession axis when the magnetic field goes in-plane because the effective g-factors $g_x^* = |g_{xx}|$ and $g_y^* = |g_{yy}|$ remain degenerate ($f_{\mathrm{R}} \to 0$ when $\theta \to 90°$). The Rabi frequency thus peaks out-of-plane but the C gate is far less efficient than the L gate for almost any

Fig. 4 | g-factors, LH mixing and extensions of the dot as a function of gate bias in the unstrained, bulk Ge device. **a** g-factors $g_\parallel$ and $g_\perp$, **b** LH mixing m^2, **c**, **d** extensions $l_\parallel$ and $l_\perp$ of the dot as as a function of V_C in the unstrained, bulk germanium device.

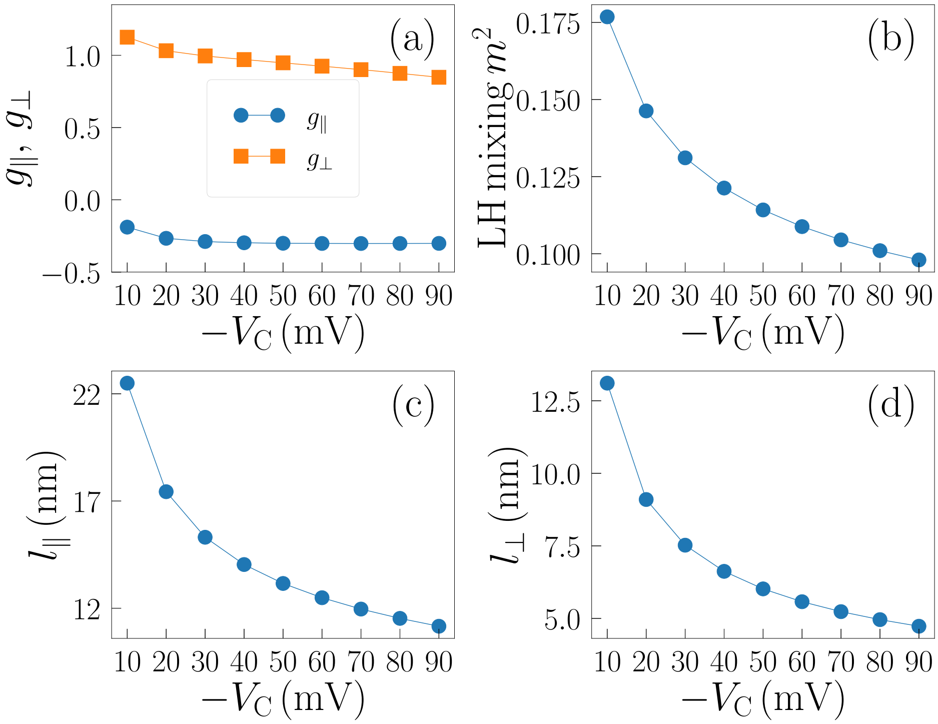

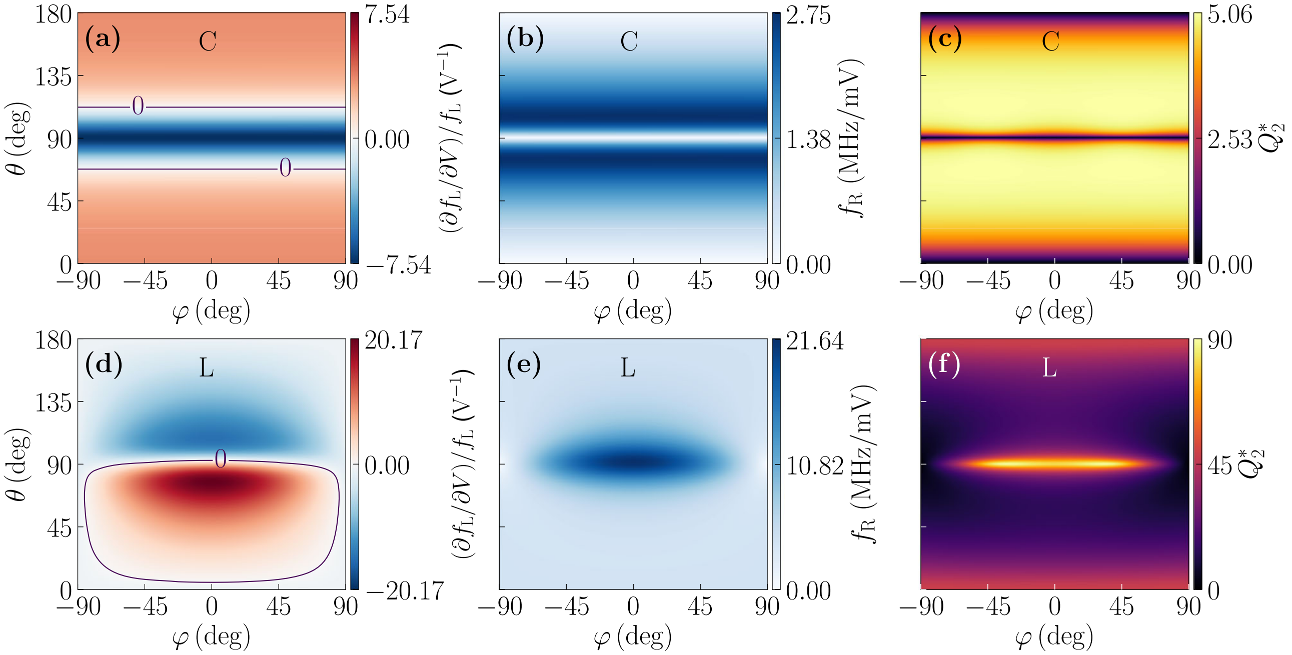

Fig. 5 | Spin manipulation metrics in the unstrained, bulk Ge device. **a**–**c** Normalized LSES $(\partial f_\mathrm{L}/\partial V)/f_\mathrm{L}$, Rabi frequency $f_\mathrm{R}/V_\mathrm{ac}$ at constant Larmor frequency $f_\mathrm{L} = 1$ GHz, and quality factor Q_2^* of the C gate as a function of the orientation of the magnetic field. **d**–**f** Same for L gate. The bias voltage is $V_\mathrm{C} = -25$ mV.

magnetic field orientation. The g' matrix of the L gate reads:

$$\hat{g}'_\mathrm{L} = \begin{pmatrix} -1.66 & 0 & 8.40 \\ 0 & -0.60 & 0 \\ 12.02 & 0 & -0.88 \end{pmatrix} \mathrm{V}^{-1}. \tag{6}$$

This matrix is dominated by the g'_{xz} and g'_{zx} terms that capture the rotations of the principal axes of the g-matrix in the inhomogeneous electric field of the L gate[37] (and the effects of the cubic Rashba interaction[35,46,47]). Namely, the axis of z' of the $g_\perp$-factor (and the orthogonal, equatorial $(x'y')$ plane) rock from left to right when the dot is driven by the L gate, which tilts the precession axis of the spin and results in coherent spin rotations at resonance. This mechanism gives rise to the prominent peak for in-plane magnetic fields, because the effects of small excursions of **B** around the effective equatorial $(x'y')$ plane are amplified by $g_\perp > g_\parallel$, and because the Rabi frequency is ∝ B, which is larger in-plane at constant Larmor frequency.

The LSES of the C gate is maximal in-plane but displays two “sweet” lines (zero LSES) at $\theta = 90 \pm 22°$[31]. Likewise, the LSESs of the side gates

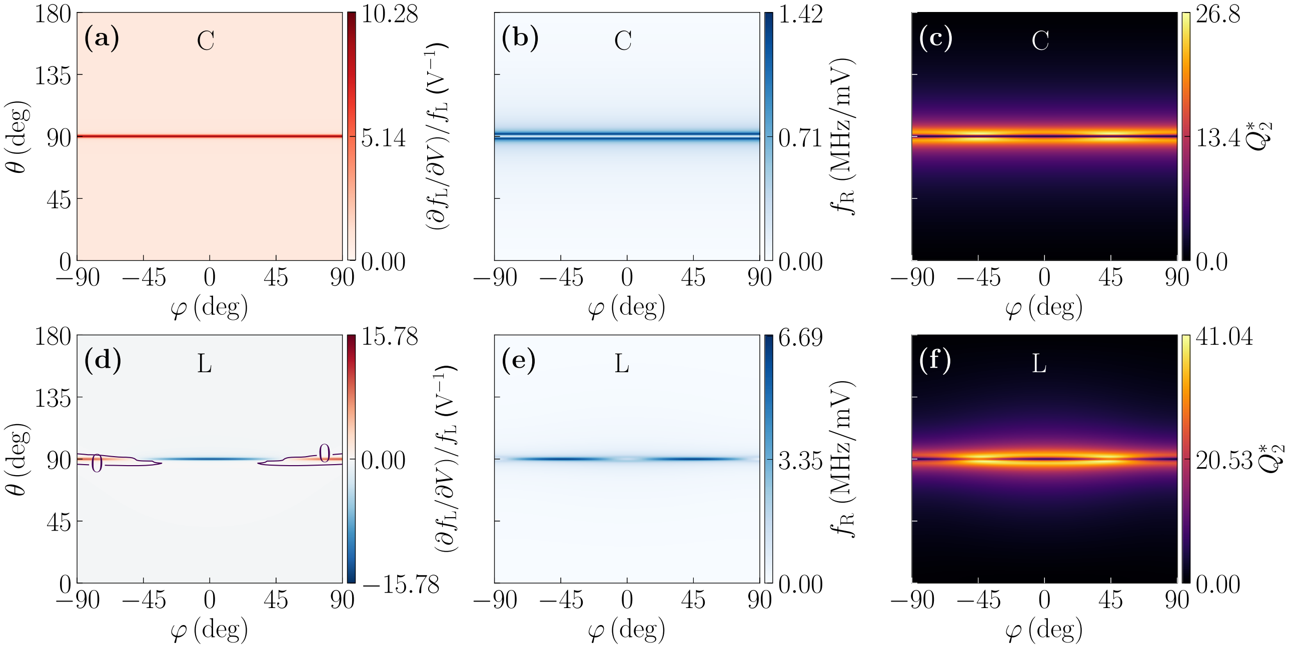

Fig. 6 | Spin manipulation metrics in a strained Ge well with thickness $L_w = 16$ nm. a–c Normalized LSES $(\partial f_L/\partial V)/f_L$, Rabi frequency f_R/V_{ac} at constant Larmor frequency $f_L = 1$ GHz, and quality factor Q_2^* of the C gate as a function of the orientation of the magnetic field. **d–f** Same for L gate. The bias voltage is $V_C = -25$ mV.

Fig. 7 | Performance metrics as a function of gate bias in the unstrained, bulk Ge device. a Rabi frequency and (**b**) quality factor of the L gate of the unstrained, bulk Ge device as a function of V_C, for a magnetic field **B**||**x**.

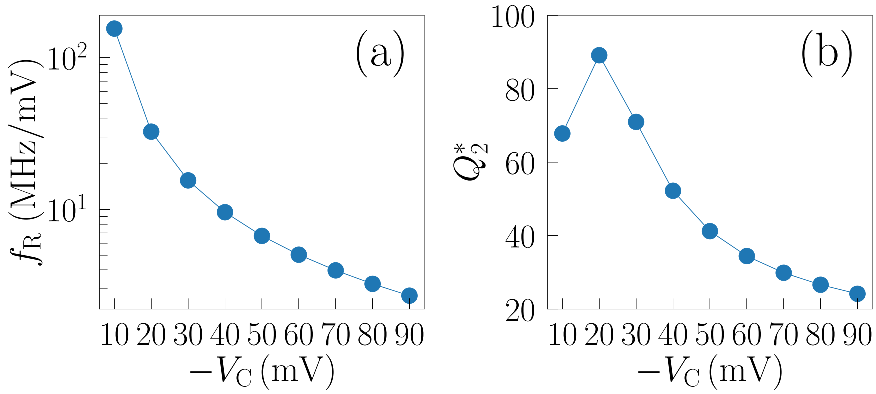

(which primarily characterize the sensitivity to lateral electric field noise) show sweet lines running near the equatorial plane. Along these sweet lines, the hole decouples (to first-order) from the corresponding component of the noise. The Rabi frequency of a given gate reaches its maximum near the sweet line(s) of that gate owing to "reciprocal sweetness" arguments[45,48]. As the C gate is inefficient in-plane, Q_2^*(C) broadly peaks for $\theta = 90 \pm 22°$, while Q_2^*(L) peaks in-plane as does the Rabi frequency. The quality factors achieved with the L gate are, nevertheless, much larger since the Rabi oscillations are faster.

The same maps are plotted in a reference, strained Ge well with thickness $L_w = 16$ nm in Fig. 6. The principal g-factors are now $g_\parallel = 0.12$ and $g_\perp = 13.64$ ($g_\perp/g_\parallel = 114$). The Rabi map is qualitatively similar to Fig. 5 for the C gate, but the LSES has no sweet lines since all diagonal elements of g'_C have the same sign[31]. The Rabi oscillations (and LSES) of the L gate are now dominated by the modulations of the diagonal g-factors because the wave function is more confined along z and thus does not "rock" as much[37]. As a consequence, the Rabi frequency still peaks in-plane but near $\varphi = \pm 45°$. All features are, however, much thinner (and closer to the equatorial plane) in the strained Ge well than in the bulk device. Indeed, the spin precession axis gets locked onto z once the magnetic field goes slightly out-of-plane in strained Ge owing to the large $g_\perp/g_\parallel$ ratio[31]. For the L gate, the full width at half-maximum (FWHM) of the Rabi peak on Fig. 5e is $\delta\theta = 39°$ and the FWHM of the Q_2^* peak on Fig. 5f is $\delta\theta = 12.3°$ (*vs* 1.7° and 4.8°, respectively, on Fig. 6e, f). Remarkably, Q_2^*(L) is optimal in-plane in the bulk Ge device, but out-of-plane in the strained Ge well, at an angle that depends on the g-factors and can thus differ from dot to dot. Also, the sweet lines of Fig. 5 are well separated from the hot spots (maximal LSES) where the sensitivity to noise is enhanced, at variance with the strained Ge well. This shall ease the alignment of the magnetic field and reduce the impact of variability on Q_2^*.

Another striking difference between the bulk device and the strained Ge well is the magnitude of the Rabi frequencies. Although the balance between the driving mechanisms is not the same, the effects of SOC are generally expected to be enhanced by a reduction of the HH/LH bandgap. For the L gate, the maximal Rabi frequency is $f_R/V_{ac} = 21.6$ MHz/mV in the bulk device but $f_R/V_{ac} = 6.7$ MHz/mV in the strained Ge well. The LSES, thus the sensitivity to noise is also enhanced, yet Q_2^* is significantly larger on average (and more broadly distributed) in the bulk device (also see the Supplementary Information for maps of Γ_2^*).

Finally, we plot in Fig. 7 the Rabi frequency and quality factor of the L gate of the bulk Ge device as a function of V_C, for a magnetic field **B**||**x**. The Rabi frequency decreases as V_C is pulled down because the dot gets smaller (see Fig. 4), thus less responsive to the drive field (and the HH/LH bandgap opens). The quality factor also decreases, but the optimal magnetic field orientation (best Q_2^*) moves towards $\varphi = \pm 45°$. Indeed, the maps of f_R and

Q_2^* remain qualitatively similar to Fig. 5, but a dip at $\varphi = 0$ progressively splits the in-plane peak of Q_2^* (owing to the different balance between the modulations of the principal g-factors and magnetic axes). For $\mathbf{B}||\mathbf{x}$, the quality factor is maximal for $V_C \approx -25$ mV.

Discussion

The above calculations illustrate the benefits in making hole spin qubits in unstrained Germanium. Without biaxial strains, the HH/LH bandgap closes and the HH/LH mixing is enhanced. The strong anisotropy of the gyromagnetic response characteristic of pure heavy-holes is, therefore, considerably reduced. The ratio $g_\perp/g_\parallel$ in the ground-state thus decreases from $\gtrsim 100$ in strained heterostructures to ≈ 3 in unstrained, bulk Ge devices. This softens the variations of the Rabi frequency, and secludes the dephasing hot spots from the dephasing sweet lines, which enables operation in a larger range of magnetic field orientations, and improves the resilience to device variability. As another asset, the density of dislocations is expected to be much lower in bulk Ge than in strained heterostructures grown on GeSi buffers.

The gyromagnetic anisotropy of unstrained, bulk Ge devices is comparable to some silicon Metal-Oxide-Semiconductor (MOS) hole spin qubits where sweet lines could indeed be resolved and harnessed[44,45]. Yet Ge spin qubits are in principle simpler to fabricate (larger dots), and are much better protected against disorder and noise in the gate stack than Si MOS devices[14,17]. The bulk Ge route may, therefore, ease the challenges of scaling to many qubits. Nevertheless, the gate stack must be more carefully engineered in bulk than in strained Ge heterostructures to limit the density of charged defects[15–17], because the top GeSi barrier will typically be thinner (≈ 20 nm) to prevent plastic relaxation.

A larger HH/LH mixing generally enhances the effects of SOC. As a consequence, the Rabi oscillations are significantly faster in unstrained, bulk Ge than in strained heterostructures, but the electrical dephasing times may be shorter (for a given level of noise). Nonetheless, the quality factors for single spin manipulation can be better in bulk Ge – namely, the Rabi frequencies increase faster than the dephasing rate in a broad range of magnetic field orientations. The hyperfine dephasing times[49] are comparable or even better in bulk Ge devices, except for strictly in-plane magnetic fields (see Supplementary Information). All germanium spin qubits would actually benefit from isotopic purification. The operation of bulk Ge qubits will likely be optimal at small Larmor frequencies f_L[24] where the single qubit operations are much faster than in strained heterostructures but the electrical $T_2^* \propto 1/B$ is long enough.

Despite the enhanced HH/LH mixing, the ground-state still exhibits a dominant HH character (LH mixing 10 to 20%). The first and higher excited orbitals (relevant for many-holes qubits[24]) may, however, exhibit much larger (even prevailing) LH components. While probing the physics of these highly mixed states is certainly interesting, reliable and reproducible results may call for a tight control of the dot occupations.

To conclude, we point out that the strength of the HH/LH mixing can be finely tuned by decoupling the compositions of the GeSi buffer and top barrier. The Ge well may indeed be grown on a thick GeSi buffer with low Si fraction, and capped with a GeSi layer with larger concentration (to achieve a robust barrier). The small compressive strains imposed by the GeSi buffer will slightly open the HH/LH bandgap and mitigate the effects of SOC (at the price of a larger g-factor anisotropy). They will also allow for a thicker GeSi barrier. The optimal buffer concentration results from a compromise between the target dephasing time T_2^* and g-factor anisotropy, thus depends on the level of noise and variability.

Methods

Computational details

The simulations are performed with the in-house TB_Sim code. The electrostatic potential in the device is calculated with a finite-volumes Poisson solver. The bias voltages on the gates are used as boundary conditions for the potential. The inhomogeneous strains due to differential thermal contraction, when relevant (see Supplementary Information), are computed with a finite-elements discretization of the continuum elasticity equations[38]. The gate stack on top of the heterostructure is made of 20 nm-thick aluminium gates laid on a 5 nm-thick Al_2O_3 oxide and surrounded by 5 nm of Al_2O_3. The hole wave functions are calculated with a finite-differences discretization of the four bands Luttinger-Kohn Hamiltonian[37–40]. All material parameters are taken from ref. 38. We use the same non-uniform, cartesian product mesh (with minimum step 5 Å) for potentials, strains and wave functions. We assume periodic boundary conditions in the (xy) plane for the potentials and strains (over a 380 nm-wide simulation box), and hard-wall boundary conditions for the wave functions (to enable the application of a finite magnetic field). The g-factors, Rabi frequencies and dephasing times are computed from the hole wave functions with the g-matrix formalism[31,41]. The bulk germanium device is simulated as a well with thickness $L_w = 170$ nm.

Data availability

Data is available from the corresponding author upon reasonable request.

Received: 6 June 2025; Accepted: 4 September 2025;

References

1. Loss, D. & DiVincenzo, D. P. Quantum computation with quantum dots. *Phys. Rev. A* **57**, 120 (1998).
2. Maurand, R. et al. A CMOS silicon spin qubit. *Nat. Commun.* **7**, 13575 (2016).
3. Froning, F. N. M. et al. Ultrafast hole spin qubit with gate-tunable spin-orbit switch functionality. *Nat. Nanotechnol.* **16**, 308 (2021).
4. Camenzind, L. C. et al. A hole spin qubit in a fin field-effect transistor above 4 kelvin. *Nat. Electron.* **5**, 178 (2022).
5. Wang, K. et al. Ultrafast coherent control of a hole spin qubit in a germanium quantum dot. *Nat. Commun.* **13**, 206 (2022).
6. Fang, Y., Philippopoulos, P., Culcer, D., Coish, W. A. & Chesi, S. Recent advances in hole-spin qubits. *Mater. Quantum Technol.* **3**, 012003 (2023).
7. Winkler, R.*Spin-orbit coupling in two-dimensional electron and hole systems* (Springer, Berlin, 2003).
8. Rashba, E. I. & Efros, A. L. Orbital mechanisms of electron-spin manipulation by an electric field. *Phys. Rev. Lett.* **91**, 126405 (2003).
9. Kato, Y. et al. Gigahertz electron spin manipulation using voltage-controlled g-tensor modulation. *Science* **299**, 1201 (2003).
10. Golovach, V. N., Borhani, M. & Loss, D. Electric-dipole-induced spin resonance in quantum dots. *Phys. Rev. B* **74**, 165319 (2006).
11. Crippa, A. et al. Electrical spin driving by g-matrix modulation in spin-orbit qubits. *Phys. Rev. Lett.* **120**, 137702 (2018).
12. Sammak, A. et al. Shallow and undoped germanium quantum wells: A playground for spin and hybrid quantum technology. *Adv. Funct. Mater.* **29**, 1807613 (2019).
13. Scappucci, G. et al. The germanium quantum information route. *Nat. Rev. Mater.* **6**, 926 (2021).
14. Martinez, B. & Niquet, Y.-M. Variability of electron and hole spin qubits due to interface roughness and charge traps. *Phys. Rev. Appl.* **17**, 024022 (2022).
15. Varley, J. B., Ray, K. G. & Lordi, V. Dangling bonds as possible contributors to charge noise in silicon and silicon–germanium quantum dot qubits. *ACS Appl. Mater. Interfaces* **15**, 43111 (2023).
16. Massai, L. et al. Impact of interface traps on charge noise, mobility and percolation density in Ge/SiGe heterostructures. https://arxiv.org/abs/2310.05902 (2023). This preprint is published as Commun. Mat. 5, 151 (2024). https://www.nature.com/articles/s43246-024-00563-8
17. Martinez, B., de Franceschi, S. & Niquet, Y.-M. Mitigating variability in epitaxial-heterostructure-based spin-qubit devices by optimizing gate layout. *Phys. Rev. Appl.* **22**, 024030 (2024).
18. Watzinger, H. et al. A germanium hole spin qubit. *Nat. Commun.* **9**, 3902 (2018).

19. Hendrickx, N. W. et al. A single-hole spin qubit. *Nat. Commun.* **11**, 3478 (2020).
20. Hendrickx, N. W., Franke, D. P., Sammak, A., Scappucci, G. & Veldhorst, M. Fast two-qubit logic with holes in germanium. *Nature* **577**, 487 (2020).
21. Hendrickx, N. W. et al. A four-qubit germanium quantum processor. *Nature* **591**, 580 (2021).
22. Lawrie, W. I. L. et al. Simultaneous single-qubit driving of semiconductor spin qubits at the fault-tolerant threshold. *Nat. Commun.* **14**, 3617 (2023).
23. Hendrickx, N. W. et al. Sweet-spot operation of a germanium hole spin qubit with highly anisotropic noise sensitivity. *Nat. Mater.* **23**, 920 (2024).
24. John, V. et al. A two-dimensional 10-qubit array in germanium with robust and localised qubit control. https://arxiv.org/abs/2412.16044 (2025).
25. Jirovec, D. et al. A singlet-triplet hole spin qubit in planar Ge. *Nat. Mater.* **20**, 1106 (2021).
26. Jirovec, D. et al. Dynamics of hole singlet-triplet qubits with large *g*-factor differences. *Phys. Rev. Lett.* **128**, 126803 (2022).
27. Zhang, X. et al. Universal control of four singlet-triplet qubits. *Nat. Nanotechnol.* **20**, 209 (2025).
28. Tsoukalas, K. et al. A dressed singlet-triplet qubit in germanium. https://arxiv.org/abs/2501.14627 (2025).
29. Wang, C.-A. et al. Operating semiconductor quantum processors with hopping spins. *Science* **385**, 447–452 (2024).
30. Wang, C.-A. et al. Probing resonating valence bonds on a programmable germanium quantum simulator. *npj Quantum Inf.* **9**, 58 (2023).
31. Mauro, L., Rodríguez-Mena, E. A., Bassi, M., Schmitt, V. & Niquet, Y.-M. Geometry of the dephasing sweet spots of spin-orbit qubits. *Phys. Rev. B* **109**, 155406 (2024).
32. Mauro, L., Rodríguez-Mena, E. A., Martinez, B. & Niquet, Y.-M. Strain engineering in Ge/Ge−Si spin-qubit heterostructures. *Phys. Rev. Appl.* **23**, 024057 (2025).
33. Stehouwer, L. E. A. et al. Germanium wafers for strained quantum wells with low disorder. *Appl. Phys. Lett.* **123**, 092101 (2023).
34. Scappucci, G., Tosato, A., Russ, M. F., Stehouwers, L. E. A. & Amir, S. Method for manufacturing a single heterojunction semiconductor device and such a single heterojunction semiconductor device, Patent WO2024210754A1.
35. Bosco, S., Benito, M., Adelsberger, C. & Loss, D. Squeezed hole spin qubits in Ge quantum dots with ultrafast gates at low power. *Phys. Rev. B* **104**, 115425 (2021).
36. Costa, D. et al. Buried unstrained Ge channels: a lattice-matched platform for quantum technology. https://arxiv.org/abs/2506.04724 (2025).
37. Martinez, B., Abadillo-Uriel, J. C., Rodríguez-Mena, E. A. & Niquet, Y.-M. Hole spin manipulation in inhomogeneous and nonseparable electric fields. *Phys. Rev. B* **106**, 235426 (2022).
38. Abadillo-Uriel, J. C., Rodríguez-Mena, E. A., Martinez, B. & Niquet, Y.-M. Hole-spin driving by strain-induced spin-orbit interactions. *Phys. Rev. Lett.* **131**, 097002 (2023).
39. Luttinger, J. M. Quantum theory of cyclotron resonance in semiconductors: General theory. *Phys. Rev.* **102**, 1030 (1956).
40. Lew Yan Voon, L. C. & Willatzen, M. (Springer, Berlin, 2009).
41. Venitucci, B., Bourdet, L., Pouzada, D. & Niquet, Y.-M. Electrical manipulation of semiconductor spin qubits within the *g*-matrix formalism. *Phys. Rev. B* **98**, 155319 (2018).
42. Michal, V. P., Venitucci, B. & Niquet, Y.-M. Longitudinal and transverse electric field manipulation of hole spin-orbit qubits in one-dimensional channels. *Phys. Rev. B* **103**, 045305 (2021).
43. Ares, N. et al. Nature of tunable hole *g* factors in quantum dots. *Phys. Rev. Lett.* **110**, 046602 (2013).
44. Piot, N. et al. A single hole spin with enhanced coherence in natural silicon. *Nat. Nanotechnol.* **17**, 1072 (2022).
45. Bassi, M. et al. Optimal operation of hole spin qubits. https://arxiv.org/abs/2412.13069 (2024).
46. Marcellina, E., Hamilton, A. R., Winkler, R. & Culcer, D. Spin-orbit interactions in inversion-asymmetric two-dimensional hole systems: A variational analysis. *Phys. Rev. B* **95**, 075305 (2017).
47. Terrazos, L. A. et al. Theory of hole-spin qubits in strained germanium quantum dots. *Phys. Rev. B* **103**, 125201 (2021).
48. Michal, V. P. et al. Tunable hole spin-photon interaction based on g-matrix modulation. *Phys. Rev. B* **107**, L041303 (2023).
49. Bosco, S. & Loss, D. Fully tunable hyperfine interactions of hole spin qubits in Si and Ge quantum dots. *Phys. Rev. Lett.* **127**, 190501 (2021).

Acknowledgements

This work was supported by the “France 2030” program (PEPR PRESQUILE-ANR-22-PETQ-0002), by the French National Research Agency (project InGeQT), and by the Horizon Europe Framework Program (grant agreement 101174557 QLSI2).

Author contributions

L.M., M.J.R. and E.A.R.M. performed the calculations. Y.M.N. initiated and supervised the work. All authors contributed to the analysis of the results and review of the manuscript.

Competing interests

The authors declare no competing interests.

Additional information

Supplementary information The online version contains supplementary material available at https://doi.org/10.1038/s41534-025-01108-8.

Correspondence and requests for materials should be addressed to Yann-Michel Niquet.